Bulletin of the Seismological Society of America, 91, 5, pp. 1112–1127, October 2001

The Importance of the Dynamic Source Effects on Strong Ground Motion during the 1999 Chi-Chi, Taiwan, Earthquake: Brief Interpretation of the Damage Distribution on Buildings

by L. A. Dalguer, K. Irikura, J. D. Riera and H. C. Chiu

Abstract The 1999 Chi-Chi, Taiwan, earthquake, that originated on a low-angle reverse fault, showed complexity and uncommon characteristics. The records show that the hanging-wall side is characterized by larger particle motions than the footwall, and the ground motion is stronger in the northern part than in the southern part of the causative fault. Although the strongest ground motion occurred near the northern part of the trace, structural damage was heavier in the southern part. In order to get a better understanding of the complex damage distribution caused by this earthquake, the dynamic rupture process was numerically simulated. Because of the differences between the observed features of the rupture process in the northern and southern parts of the fault, each part was modeled independently by using a 2D discrete element model (DEM). The principal results of the simulation show that the velocity ground motions in the northern part, in the frequency range of 0.5–2 Hz (natural frequency range of standard structures), are small near the surface break, thus, light structural damage might be predicted near the surface rupture. Moreover, in the northern part the fault rupture propagation reaches the surface with a very slow velocity (about 1.2 km/sec); however, in the southern part the rupture propagation reaches the surface with higher velocity (about 3.0 km/sec). These differences between the models could explain why the ground motion near the surface rupture in the northern part caused less damage in structures than the ground motion in the southern part.

Introduction

Due to its complexity and uncommon characteristics, the Chi-Chi, Taiwan, earthquake (M_w 7.6) of 20 September 1999 had a great impact on the international community of scientists and engineers devoted to seismology and earthquake engineering. The earthquake originated on a low-angle reverse fault with a strike of nearly N5°E and a dip between 25° and 36° (Shin *et al.,* 2000). The rupture of the causative fault reached the surface and propagated along about 80 km, starting in the south and extending northward on the Chelongpu fault, as shown in Figure 1. Spectacular horizontal displacements up to 9.0 m and vertical offsets of 1.0 to 8.0 m were registered along the surface rupture. The earthquake was one of the most destructive and largest earthquakes of this century in Taiwan. The death toll was 2333, with 10002 people injured (Shin *et al.,* 2000). The epicenter of this shallow earthquake was located near the small town of Chi-Chi (23.87N, 120.75E), 150 km (90 miles) south of Taipei. In order to analyze the damage distribution caused by the earthquake, the northern and southern zones are defined as shown in Figure 2a and b. Although the stations records show that the strongest ground motion and the largest displacements were located in the northern part of the Chelongpu fault, structural damage in that area appears to be less than in the southern portion. In fact, only buildings directly on the surface rupture had severe damage in the northern zone. In general, the most severe damage on buildings caused by the ground shaking was registered in the hanging wall and was greater in the southern part than in the northern portion (Fig. 2a). From the distribution of damaged structures, shown in Figure 2a, and the population distribution along the causative fault, shown in Figure 2b, we can observe that the northern part of the fault (except for its final portion) has higher population density than the southern part (near the epicenter area); however, damage is larger in the southern part. Such difference in the damage distribution can be inferred from Figure 3, which shows a comparison of the spectral pseudovelocity from records of stations located in the north (TCU052) and south (TCU129 and TCU089). The peak velocity for frequencies less than 1.0 Hz is larger in the northern part. On the contrary, for frequencies greater

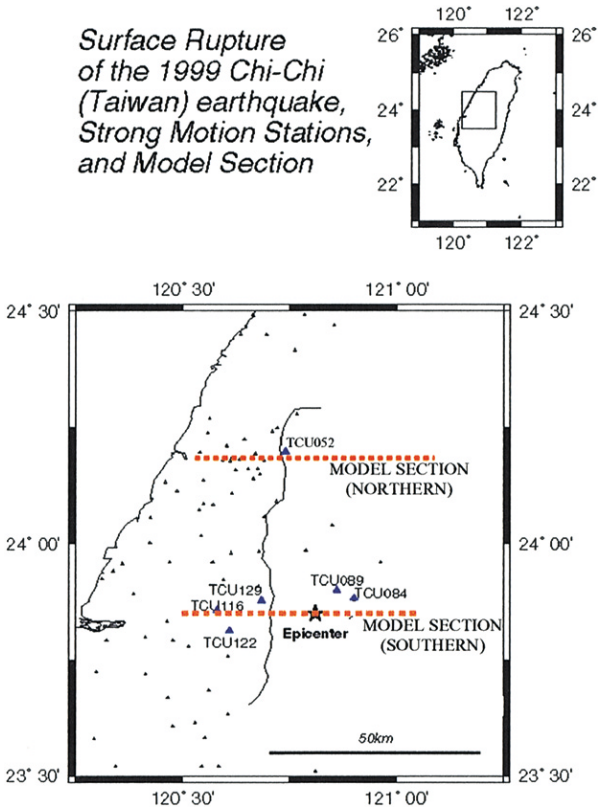

Figure 1. Location of the surface rupture of the Chelongpu fault; stations records used for comparison and sections of the northern and southern model.

than 1.0 Hz, the peak velocity ground motion is larger in the southern part. This means that the northern region generated stronger ground motion at low frequencies than did the southern region. Figure 2a also shows the highest concentration of damage in a small area at the end of the fault in the northern part, where the rupture of the fault stopped, turning suddenly to the east. This region of the fault is out of our scope because of its particular complexity, escaping from the purpose of this article to explain the general damage distribution caused by the earthquake.

In order to better understand the complex damage distribution caused by this earthquake, we performed a numerical simulation of the dynamic rupture process. Since the faulting process appears to have been nearly pure thrust along the various fault segments, a 2D discrete element model (DEM) was employed to perform a dynamic simulation of the rupture process and of the near-fault ground motion. On account of the differences in the observed features of the rupture process in both parts of the fault, each part was modeled independently. The dynamic rupture process simulation of the southern part was already presented by the authors in a previous article (Dalguer *et al.,* 2001). In this article we simulated the mechanism of the reverse fault near the hypocentral area, as well as the near-source ground motion, the results obtained closely matching the observed ground-motion records. We showed that this kind of fault generates large differences between the near-source ground motions on the hanging wall and on the footwall. The ground motions on the hanging wall are larger than in the footwall, and the numerical simulation suggests that such a difference is principally caused by the asymmetric geometry of the hanging wall and footwall. For this earthquake, where the rupture of the fault reaches the surface, the effect of the asymmetry on the ground motion is considerable. The characteristics of this kind of earthquakes (dipping fault) were also shown by Mikumo and Miyatake (1993) in their investigation of the dynamic rupture process of the 1961 Kita-Mino earthquake in central Japan and by previous theoretical dynamic simulation of dipping fault, for example Nielsen (1998), Shi *et al.* (1998), Oglesby *et al.* (1998, 2000), as well as that observed in the foam rubber experiment of a thrust fault presented by Brune (1996).

Dynamic Model

Several attempts to perform numerical analyses of the dynamic rupture processes of a fault have been described in the literature. The pioneering work of Kostrov (1966) simulated the spontaneous propagation of an anti-plane shear crack. Das and Aki (1977) and Andrews (1976), using the slip-weakening model as a friction law of the fault, simulated spontaneous rupture propagation of an in-plane shear crack. Subsequently, the rupture process of the fault was simulated with more sophisticated models (e.g., Mikumo and Miyatake, 1978; Day, 1982a,b; Virieux and Madariaga, 1982; Cochard and Madariaga, 1994, Fukuyama and Madariaga, 1998; Inoue and Miyatake, 1998; Madariaga *et al.,* 1998). Dynamic models are frequently used to study the physics of earthquakes, as related to the rupture process of the fault. Although few efforts were devoted to the simulation of ground motion based on dynamic models, some recent contributions should be cited. Olsen *et al.* (1997) simulated the rupture process and near field ground motion of the 1992 Landers (California) earthquake using a finite-difference method in the frequency range 0.1 to 0.5 Hz. Inoue and Miyatake (1998) simulated theoretical strong ground motion generated from the rupture process on a shallow strike-slip fault using a 3D finite-difference method in frequencies up to 2.0 Hz.

In this article, we simulate the rupture dynamic of a preexisting fault and near-source ground motion, solving the elastodynamic equation of motion using the discrete element method (DEM). The DEM is widely employed in engineering to designate lumped mass models in a truss arrangement, as opposed to finite element method (FEM) models that may also consist of lumped masses, but normally require to mount a full stiffness matrix for response determination. The term has also been used for models of solids consisting of assemblies of discrete elements, such as spheres in elastic contact, employed in the analysis of perforation or penetration of concrete or rock. It should be noted that the desig-

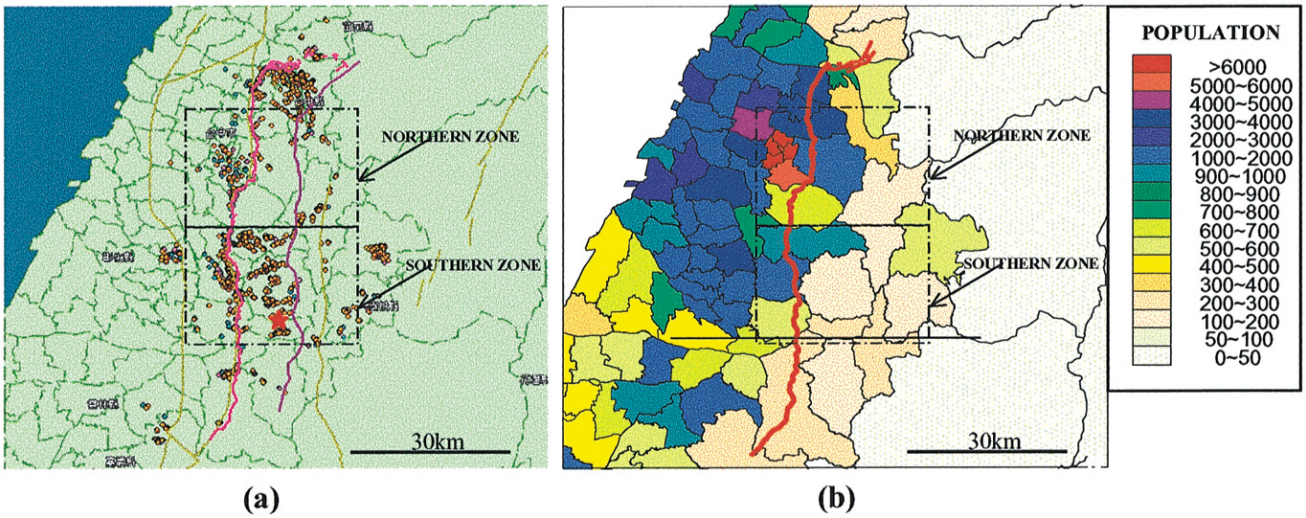

Figure 2. (a) Damage distribution of buildings in Nantou and Taichung area: orange dots show completely damaged areas and green dots show severely damaged areas (Architecture & Building Research Institute, Ministry of Interior, ROC, Taipei, Taiwan); (b) Population distribution along the causative fault (Tsai and Huang, 2000). The red line represent the Chelungpu fault (causative fault of the 1999 Chi-Chi earthquake), and the purple line in part a is the Shuangtung fault.

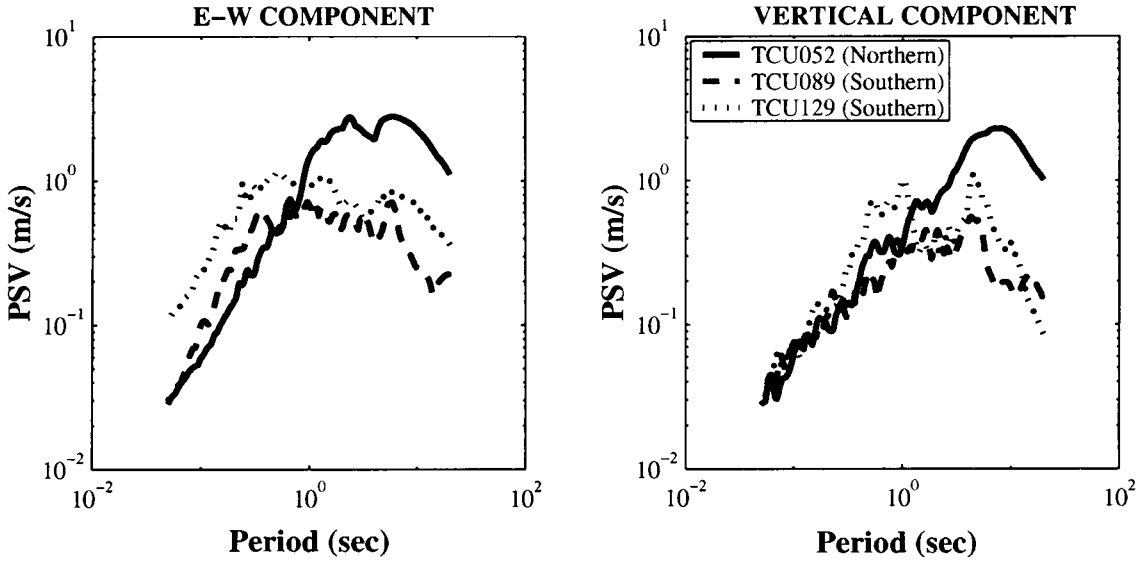

Figure 3. Comparison of pseudo–spectral velocity for records of stations at the northern and southern parts.

nation *lattice models,* common in physics, may be more adequate, although it omits reference to a fundamental property of the approach, which is the lumped-mass representation. In the present DEM formulation, orthotropic solids are represented by a three-dimensional periodic trusslike structure using cubic elements as shown in Figure 4. This model is based on earlier developments in aeronautical engineering in which, for purposes of structural analysis, it is often necessary to establish the equivalence between trusslike structural systems and a continuous medium. Nayfeh and Hefsy (1978) established the equivalence requirements between the cubic arrangement shown in Figure 4 and an orthotropic elastic medium. The method leads to results that converge to solutions for a linear elastic continuum in dynamic problems. Riera and Rocha (1991) used the approach in fracture studies, Doz and Riera (1995) employed the method to model the stick-and-slip motion along friction surfaces, Dalguer *et al.* (1999) evaluated the foreshock and periodicity of earthquakes, and Dalguer *et al.* (2001) modeled a fault dynamic rupture using the slip-weakening friction model to

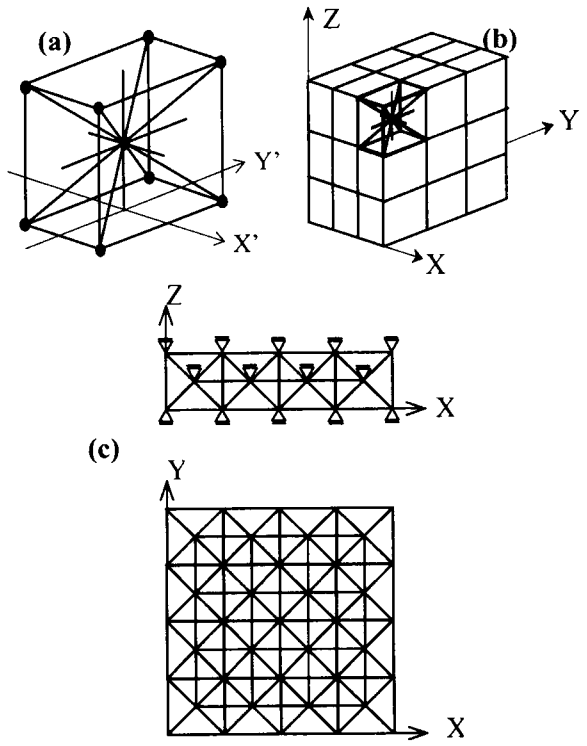

Figure 4. Numerical model used for the dynamic simulation (DEM): (a) basic cubic module, (b) generation of prismatic body, and (c) representation of a plate-strain state (no z displacements).

simulate the rupture process of the hypocentral area of the 1999 Chi-Chi (Taiwan) earthquake. Also Mora and Place (1994), Shi *et al.* (1998), and Rimal (1992) used a 2D lattice model similar to the DEM to simulate dynamic rupture of earthquake faulting.

In the case of an isotropic elastic material, the cross-sectional axial stiffness of the longitudinal bars in the equivalent discrete model is given by:

$$AE_{\mathrm{n}} = \phi EL^2, \text{ bar length } = L, \tag{1}$$

while for the diagonal bars,

$$AE_{\mathrm{d}} = 2\delta\phi E\,\frac{L^2}{\sqrt{3}}, \text{ bar length } = \sqrt{3}\,\frac{L}{2}, \tag{2}$$

where for approximately isotropic solids, namely, solids with equal stiffness in the three orthogonal directions, $\phi = (9 + 8\,\delta)/(18 + 24\,\delta)$, $\delta = 9v(4 - 8v)$, v is the Poisson's ratio, and E is the Young's modules of the material. For other situations, for example layered (orthotropic) rocks, the aforementioned constants take on other values (See Nayfeh and Hefsy, 1978). It should be stressed that no lattice or trusslike model can exactly represent a locally isotropic continuum, and for that matter it can also be argued that no locally isotropic continuum exists. Isotropy in solids is a bulk property that reflects the random distribution of the orientation of constituent elements. Details of the calculation of the equivalent cross-sectional axial stiffness of the normal (AE_{n}) and diagonal (AE_{d}) elements for a cubic lattice array given by equation (1) and (2) respectively are presented in the Appendix.

In the discrete dynamic model, masses are concentrated at nodal points. As shown in Figure 4a, solids are represented as an array of normal and diagonal bars linking lumped nodal masses. The dynamic analysis is performed using explicit numerical integration in the time domain. At each step of integration a nodal equilibrium represented by equation (3) is solved by the central finite-differences scheme.

$$m\ddot{u}_i + c\dot{u}_i = f_i, \tag{3}$$

where m denotes the nodal mass, c is the damping constant, u_i, $\dot{u}_i$, $\ddot{u}_i$ denote a component displacement, velocity, and acceleration, respectively, of the nodal coordinates vector, and f_i denotes a component of the resultant forces at one nodal point including elastic, external, and frictional forces in direction i of the motion. In the current model, only the nodal points that coincide with the preexisting fault, once it breaks, are under frictional force governed by any predefined friction law. The damping constant c was assumed to be proportional to the rigidity k of the bars of every cubic element, that is $c = d_f k$, where d_f was assumed to be 0.005. It is approximately a critical damping ratio (χ) less or equal to 0.045.

Equation (3) represents the equation of motion of a discrete point in the continuum. When this point is on the preexisting fault, the fault parallel component of the resultant force (f_i) is governed by the constitutive relation on the fault.

Friction Law on the Fault

Laboratory experiments on rock (e.g., Dieterich, 1979; Ohnaka *et al.,* 1987, Ruina, 1983) lead to slip- and/or rate-dependent friction models. In the present model we adopt the simple slip-weakening friction model that was first proposed by Ida (1972) and extensively used for dynamic simulation of fault rupture processes (e.g., Andrews, 1976; Day, 1982b; Olsen *et al.,* 1997; Fukuyama and Madariaga, 1998; Harris and Day, 1999). The slip-weakening friction model is schematically represented in Figure 5. The shear force calculated from the resultant force, f_i, of equation (3) could be expressed by the shear stress, τ. The following is the relation between the shear stress, τ, and the slip of the fault, u.

$$\begin{aligned} &\tau < \tau_u, && \text{for } u = 0,\\ &\tau = -\frac{\tau_u - \tau_{\mathrm{f}}}{D_{\mathrm{c}}}\,u + \tau_u && \text{for } 0 < u < D_{\mathrm{c}},\\ &\tau = \tau_{\mathrm{f}} && \text{for } u \geq D_{\mathrm{c}}, \end{aligned} \tag{4}$$

where τ_{u} is the critical stress or the upper yield point, τ_{f} is the final stress or the residual stress, which is considered as

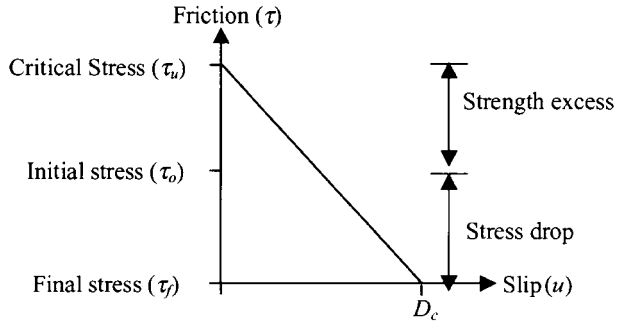

Figure 5. The slip-weakening friction model.

the dynamic friction stress level, and D_c is the slip required for stress to drop to its dynamic friction level. We assume that there is not back slip on the fault, which means that the slip velocity is always greater or equal to zero.

In order to verify the adequacy of our approach, using the DEM, to simulate a dynamic rupture process, we analyzed the spontaneous inplane rupture with the slip weakening law employed by Andrews (1976). In this problem, plane strain is assumed. The crack plane is the x-y plane, in which the crack propagates bilaterally in the x direction and extends indefinitely in the y direction. The medium is thus an infinite, homogeneous, isotropic, and linearly elastic crack plane. As indicated before, the rupture assumes a slip-weakening law. When the crack propagates, it will not stop.

For the numerical computations, the parameters are normalized as follow (Andrews, 1976): Shear stress along the crack plane $\tau' = \tau/\Delta\tau$, x axis parallel to the crack plane $x' = x/L_c$, time $t' = t\beta/L_c$; slip: $u' = u\mu/L_c\Delta\tau$; slip velocity: $v' = v\mu/\beta\Delta\tau$, where β is the S-wave velocity, μ is the shear rigidity, $\Delta\tau$ is the stress drop, and L_c is the critical half-length of a Griffith crack in plane strain derived by Andrews (1976),

$$L_c = \frac{8\mu(\lambda + \mu)G}{\pi(\lambda + 2\mu)(\tau_o - \tau_f)^2}, \quad (5)$$

where λ and μ are the Lamé constants, and G is the effective fracture surface energy given by

$$G = \frac{1}{4}(\tau_u - \tau_f)D_c. \quad (6)$$

We assume that that Poisson's coefficient is 0.25, so $\alpha/\beta = \sqrt{3}$, where α is the P-wave velocity. These nondimensional quantities are equivalent to assuming that $\mu = 1$, $\Delta\tau = 1$, $\beta = 1$, $\alpha = \sqrt{3}$, $L_c = 1$, density $\rho = 1$. The calculations were performed with a grid size $\Delta x = 0.1L_c$ (length of the side of one cubic element) and $(\tau_u - \tau_o)/\Delta\sigma = 0.8$. Using equations (5) and (6), $\Delta_c = 1.31$.

The numerical solution is obtained for the near-field elastodynamic motion coupled to frictional sliding on a prescribed crack plane. Initially the stress distribution along the fault is in the initial stress level (τ_o) shown in Figure 5, the rupture is initiated artificially by imposing a stress drop to propagates at least as fast as 0.5β, which leads to initial stresses along the fault that increase monotonically without any relative slipping along the fault. Eventually, the interface shear stress (τ) at a point exceeds the local shear strength (critical stress level τ_u) and slip at a node occurs, governed by the slip weakening model shown in Figure 5 and represented by equation (4). Considering that the seismic radiation depends only on the stress change (stress drop) during the earthquake, and not on the total stress, we assume that the initial stress (τ_o) along the fault is at its zero level. Therefore, the necessary parameters required to simulate the rupture process governed by the slip-weakening friction model are the strength excess, stress drop, and critical slip.

Figures 6 shows the results of our numerical simulation for a theoretical spontaneous inplane rupture problem analyzed by Andrews (1976). The results are very consistent with the solution presented by Andrews (1976). Figure 6a shows the space–time distribution of rupture. The region between the two solid lines is the rupture front, where slip velocity is nonzero and stress drop is incomplete. Figure 6b shows the slip velocity as a function of position at the same instant, at dimensionless time $\beta t/L_c = 12.36$. Figure 6c–f shows the shear stress and slip as a function of position on the crack plane at dimensionless time $\beta t/L_c = 8.07$, 10.38, 12.36, and 14.34, respectively. The peak of the shear stress on the rupture front as well as the secondary peak associated with the S waves are very precisely described by the DEM.

Assumptions in the Numerical Simulation to Simulate the 1999 Chi-Chi Earthquake

Because of the differences in the observed features of the rupture process in the northern and southern parts of the causative fault of the 1999 Chi-Chi earthquake, each part was modeled independently. The problem is tackled in a plane-strain condition. The location of the two models sections along the surface rupture is shown in Figure 1. The first model (southern part) is near the epicentral area, and the second model (northern part) is near the TCU052 station. The parameters used for the dynamic simulation and the geometry of the two fault models are shown in Figure 7. The fault model of the southern part is the same used by Dalguer *et al.* (2001). Both models share the following common assumptions:

1. There is a surface sedimentary layer with a depth of 4 km characterized by a set of P-wave velocity (4.3 km/sec), S-wave velocity (2.5 km/sec), density 2500 kg/m$_3$, corresponding to Young's modulus 3.9×10^{10} N/m^2, shear modulus 1.56×10^{10} N/m^2 and Poisson's ratio 0.25. The basement (seismogenic zone) is a homogeneous medium with P-wave velocity (6.1 km/sec), S-wave velocity (3.5 km/sec), density 2700 kg/m^3, corresponding to Young's

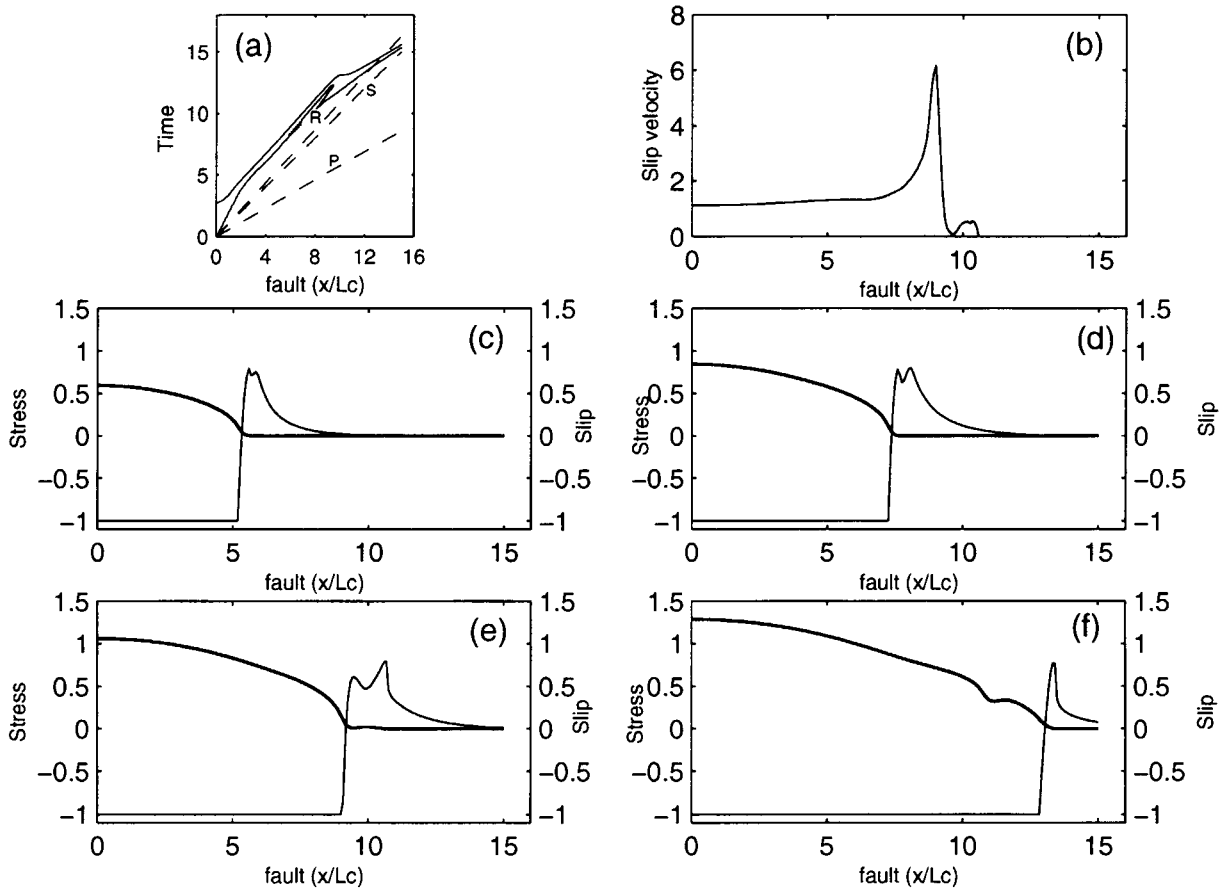

Figure 6. Dynamic solution, resolved by the DEM, of the spontaneous inplane rupture problem presented by Andrews (1976). (a) Space–time of rupture propagation. Region between the two solid lines is the rupture front, where slip velocity is nonzero and stress drop is incomplete. Dashed line labeled P, S, and R represents the wave front of the compressional, shear, and Rayleigh waves, respectively, as a reference (Rayleigh wave velocity = 0.9194β). (b) Dimensionless slip velocity, $v' = v\mu/\beta\Delta\tau$, as a function of position on the crack at time the dimensionless time $\beta t/L_c = 8.07$. Shear stress and slip as a function of position on the crack plane at dimensionless time $\beta t/L_c =$ (c) 8.07, (d) 10.38, (e) 12.36, and (f) 14.34, respectively. Heavier solid curve is dimensionless slip function divided by 10, $\mu u/10L_c(\Delta\tau)$; lighter solid line is the dimensionless change of shear stress, $(\tau/\Delta\tau)$.

modulus 8.37×10^{10} N/m^2, shear modulus 3.35×10^{10} N/m^2, and Poisson's ratio 0.25.

2. The preliminary report of the 1999 Chi-Chi earthquake (Shin *et al.,* 2000), suggests a focal depth of 7–11 km and dip of 25°–36°. We selected a dip of 33°41′ in order to have an integer element size of the DEM to model the free surface. The hypocenter is located at a depth of 8.5 km.
3. The slip-weakening friction model is adopted as the constitutive relation for the fault.
4. The stress drop along the fault plane in the shallow surface layer is negligible.
5. The ultimate stress, that is, the strength excess on the fault surface in the shallow surface layer increases linearly with depth and, in order to avoid any fault opening, we applied a normal stress along the fault, equivalent to the strength excess.

The choice of the parameters used for the simulation of the dynamic rupture of a fault is a delicate issue, still subject to debate. The author's experience, nevertheless, suggests that, in general, it is very unlikely that essentially correct simulated response will result from essentially incorrect models or parameters. For the assumption of a slip-weakening friction law, we need to define the stress drop, the strength excess, and the critical slip, D_c, along the fault. The stress drop can roughly be defined from the results of the kinematic inversion of ground motion, so we can guess approximate asperities area (we assume that asperity is a zone of higher stress drop than surrounding areas). The

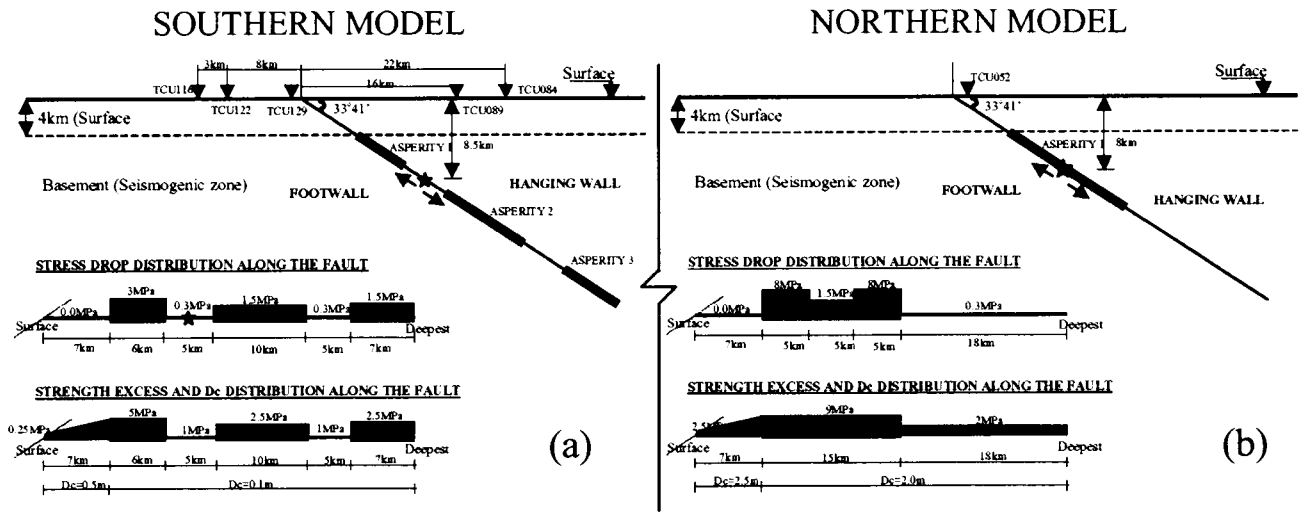

Figure 7. Fault models and parameters distribution used for the dynamic simulation: (a) southern model, (b) northern model.

choice of D_c and the strength is quite difficult, since there is no way to get them from observations, and there may be various combinations that fit the data. This is in accordance with the conclusion from Guatteri and Spudich (2000), who indicate that there is no unique solution to select D_c and strength excess. But in general, we can get some information on D_c from several laboratory experiments and field analyses. Ohnaka (1992) reported that D_c is constant within the brittle layer, Marone and Kilgore (1993) proposed that D_c is larger when a fault gouge zone is thicker, so, the rupture in the shallow crust is stable due to the presence of a large amount of gauge materials between the fault zone. And also, from the report of Ide and Takeo (1997) who study the stress change on the fault during the dynamic rupture propagation in the 1995 Kobe earthquake through seismic inversion, D_c is more than 1.0 m in the shallow crust and about 10 cm in the brittle layer. From our numerical experiments, we observed that the frequency content of the ground motion is related to the rupture propagation velocity, a high rupture velocity producing higher frequencies than a slow velocity. The rupture velocity is related to D_c and the strength excess, that is, small D_c and strength excess produce higher rupture velocity than large D_c and strength excess. In view of the preceding arguments, the modeling procedure in the article was as follows: from kinematical inversion results, we can roughly get the asperities areas and the stress drops. The preliminary results of kinematical inversions (e.g., Iwata *et al.,* 2000; Ma and Mori, 2000; Yagi and Kikuchi, 2000) show the existence of larger asperity located in the northern part and relatively two or three small asperities in the southern part. The D_c and strength excess were selected in order to fit the damage pattern, that is, define combination of D_c and strength excess in order to explain in a general way the difference of the ground motion between the northern and southern zone of the fault. Considering these observation, and the arguments given previously, we start from the assumption that D_c is larger near the free surface than at higher depths and that it is larger in the northern region that in the southern region. Therefore, in the model for the southern part, the existence of three asperities with relatively small widths (about 7 km) and stress drop between 1.5 MPa and 3 MPa were used in the basement underlying the sediments, and the critical slip 0.5 m in the surface layer and 0.1 m in the deep part (Fig. 7a). The northern part, on the other hand, is assumed to have just one asperity with larger width (15 km) and higher stress-drop (between 1.5 MPa and 8 MPa), the critical slip is 2.5 m in the surface layer and of 2.0 m in the deep part (Figure 7b).

The fault models are constructed taking into account the two sides of the fault. We assume that the fault has a thickness equivalent to the size of one cubic cell. Once the fault breaks, the linkage between the two surfaces of the fault is broken, being governed by the friction law. The shear stresses on both sides of the fault are equal in magnitude but act in opposite directions. The models used for the simulation (Fig. 7) include a preexisting fault 40 km wide in a solid of 66 km $\times$ 28.25 km. 29832 cubic cells with 0.25 km long sides were needed to construct the 2D model space bounded by a free surface and three artificial boundaries that simulate the semiinfinite space. Viscous dampers were introduced on the artificial boundaries in order to avoid the reflection of waves from the edges of the domain of computation. The boundary conditions at the surface were specified as zero shear and normal stresses. During the rupture process, only the inertial stresses caused by the dynamic motion act on the surface. For the numerical integration of the equation of motion, a time step of 0.05 sec was used.

Simulation Results and Discussion

The two fault models present similar characteristics, that is, the results of the dynamic rupture process of the two models illustrate the dynamic effects of a thrust faulting on the ground motion. The main characteristics of dipping faults that breaks the surface are that the slip of the fault and the ground motion is larger in the hanging wall than in the footwall. As we analyzed in a previous article, where we simulated the dynamic rupture process of the southern part (Dalguer *et al.,* 2001), the large difference in the near-source ground motion between the hanging wall and footwall is caused mainly by the asymmetric geometry of the hanging wall and footwall. We also concluded that the effect on the ground motion of the rupture reaching the surface is strong near the surface break of the fault, because the radiated waves are trapped in the hanging wall, resulting in the amplification of the ground motion in the wedge of the hanging wall.

The slip and slip velocity distribution along the fault shown in Figure 8a (southern model) and b (northern model) suggest that the total slip duration along the fault and the final slip are larger in the northern model than in the southern model. The peak slip velocity in the asperities of the fault of the southern model is reached suddenly as a damped step function. This is similar to the Kostrov's pulse (Kostrov, 1964) that was theoretically obtained in a self-similar shear-crack propagation. Nevertheless, although the northern model also shows this sudden increase of the slip velocity in the beginning of the rupture, the peak value is reached smoothly after passing this sudden step. These results suggest that the rupture process in the southern model is rougher than in the northern model, despite the fact that the slip velocity near the surface is larger in the northern model than in the southern model, as shown in Figure 9, which shows the space–time distribution of slip velocity of the southern and northern model.

The comparison of the rupture propagation (Figure 10) shows that the rupture of the northern model crosses the asperity with supersonic velocity and suddenly changes to subsonic velocity when it leaves the asperity. The rupture velocity toward the free surface reaches small values between 0.9 km/sec and 1.8 km/sec, being the smallest near the free surface. Toward the deeper part, the rupture reaches velocities equivalent to the *S*-wave velocity, after leaving

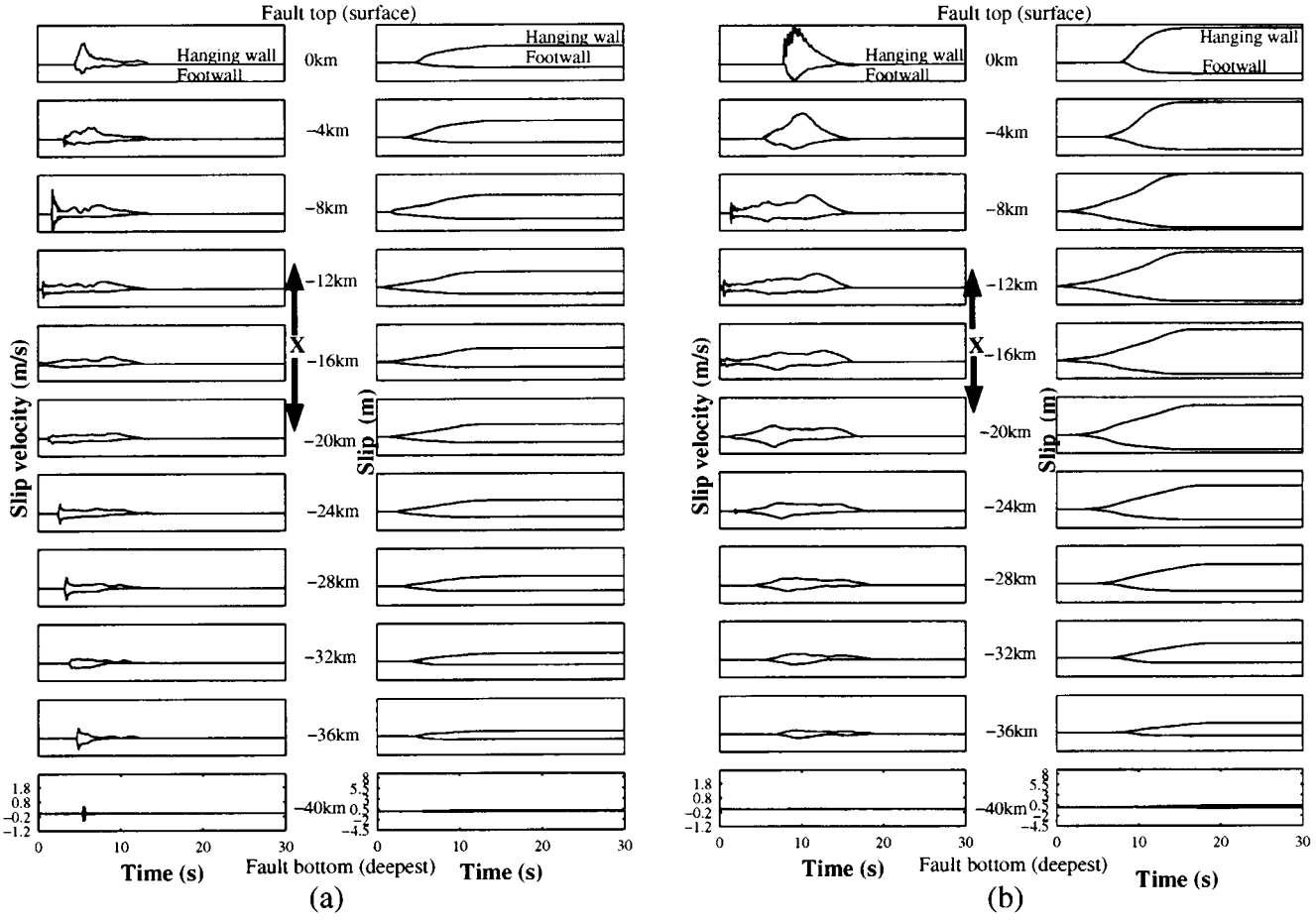

Figure 8. Slip and slip velocity along the fault: (a) southern model, (b) northern model.

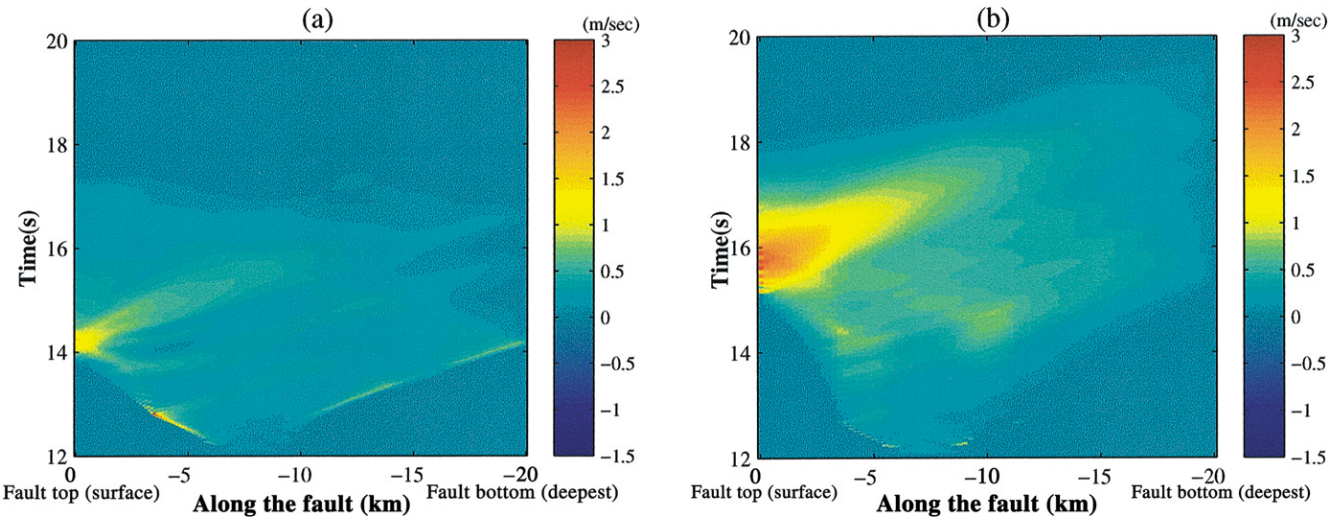

Figure 9. Space-time of slip velocity: (a) southern model, (b) northern model.

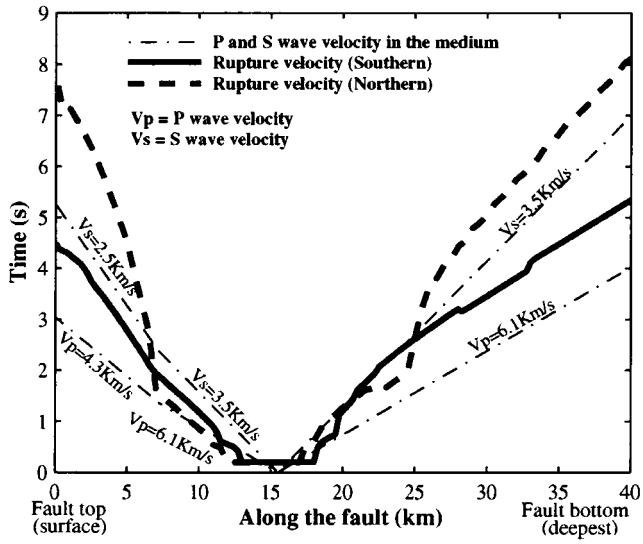

Figure 10. Comparison between the northern and southern model of the space–time of rupture propagation.

the asperity. On the other hand, the rupture of the southern model reaches velocity equivalent to the *S*-wave velocity toward the free surface, but near the free surface the rupture accelerates reaching supersonic velocity. Similarly, toward the deeper zone, the rupture starts with subsonic velocity and increases monotonically reaching supersonic velocity in the deepest part of the fault. These results suggest that the rupture velocity in the northern model propagates slower than that of the southern model. The major difference is near the free surface where the rupture velocity of the northern model reaches in average 1.2 km/sec, while the southern model reaches on average 3.0 km/sec.

The comparison of the ground motion on the surface between the northern and southern model (in a frequency range up to 2.00 Hz) is shown in Figures 11 and 12. Figure 11 shows the final displacements, peak velocity, and peak velocity in a frequency range of 0.5 to 2.0 Hz. Figure 12 shows the waveforms of the velocity ground motion in a frequency range of 0.5 to 2.0 Hz. Figure 11a and h shows that the final displacement and the peak velocity are larger in the northern model than in the southern model. These results show that the southern model predicts a vertical displacement around 2.0 m and a horizontal displacement around 3.5 m on the hanging wall; on the other hand, the northern model predicts a vertical displacement around 4.0 m and a horizontal displacement around 6.5 m on the hanging wall. However, when the ground-motion velocities are filtered in a frequency range of 0.5 to 2.0 Hz, as shown in Figures 11c and 12, the peak velocities are larger in the southern model than in the northern model (Fig. 11c), and also, the waveforms of Figure 12 show that the southern model contains shorter wavelengths than the northern model, especially on the hanging wall. These results suggest that the northern model predicts stronger ground motions than the southern model for lower frequency. On the other hand, in a higher frequency range, between 0.5 and 2.0 Hz (natural frequency range of standard structures: 1–4 story), the ground motion is stronger in the southern model. From these results we can conclude that although the northern model presents stronger ground motions, the most severe damage in structures should occur in the southern model, which is more likely to severely excite the lower modes of standard structures.

This differences of ground-motion intensity and predominant frequency between the northern and southern model may be due to the effects of the dynamic parameters of the source used for the simulation, that is, the resistance of the fault (strength excess) and critical slip that are larger

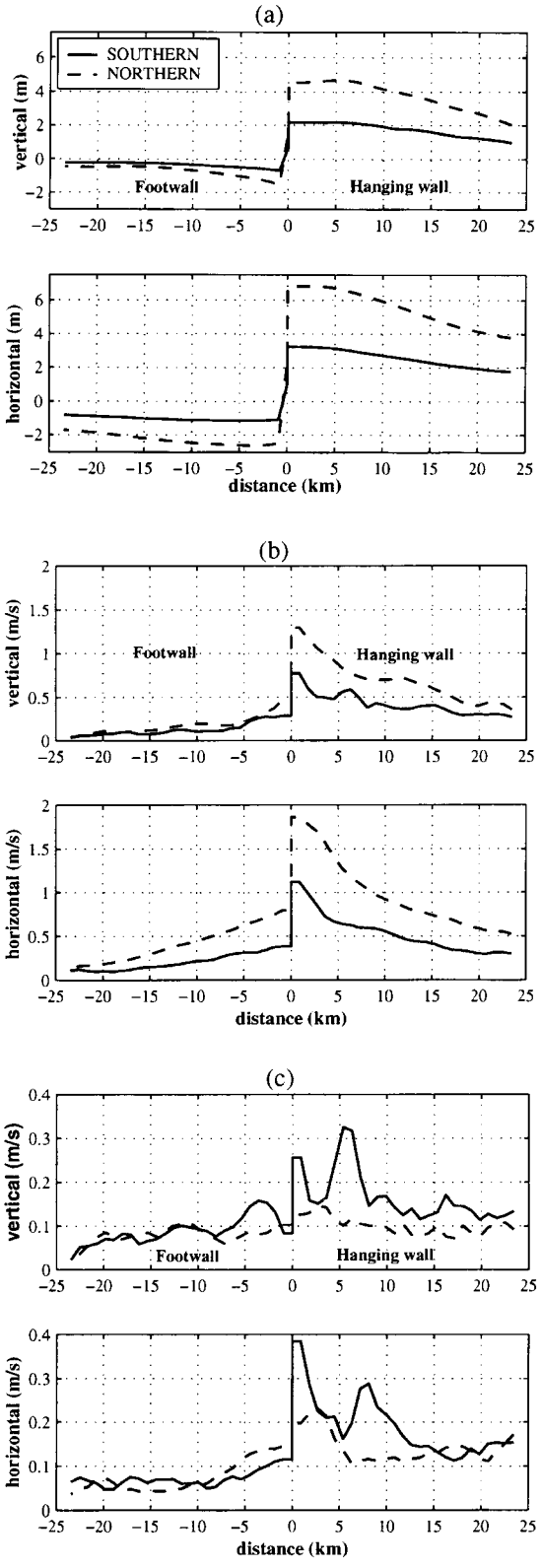

Figure 11. Comparison of the final displacement and peak velocity on the surface between the northern model and southern model: (a) final displacement, (b) peak velocity, (c) peak velocity in a frequency range of 0.5–2.0 Hz.

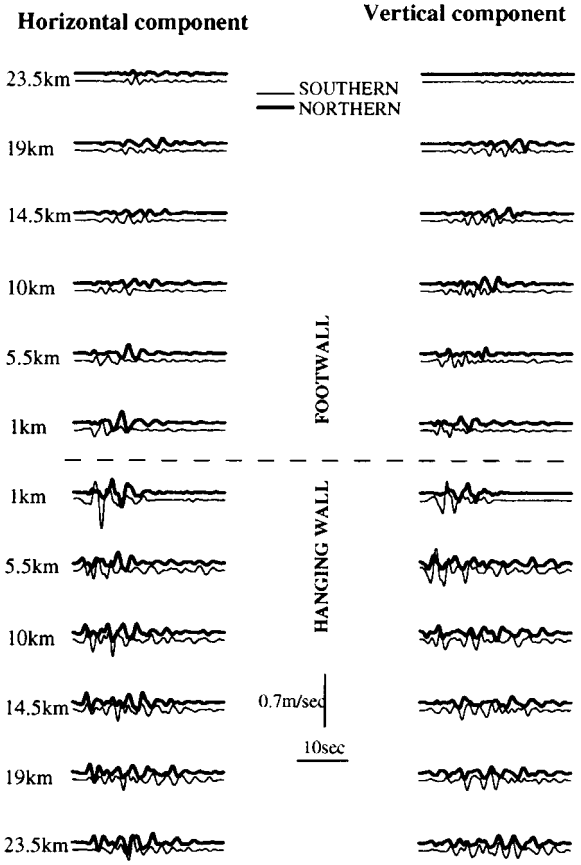

Figure 12. Comparison between the northern and southern model results of the waveforms of the velocity ground motion in a frequency range of 0.5–2.0 Hz.

in the northern model than in the southern model. When these parameters increase in magnitude, the rupture process of the fault is delayed, causing slower rupture velocity as shown in Figure 10, where the rupture propagation of the northern model is slower than that on the southern model. The critical slip also affects the beginning of the slipping process. In this zone of the slip, called the breakdown zone, the slip velocity reaches its peak as a damped step function similar to the Kostrov's pulse, and the magnitude of this peak increases when the critical slip decreases. This effect could be observed in Figure 8a (southern model) and b (northern model). These figures show that this peak is larger in the southern model than in the northern model, even though the northern model fault has a larger stress drop. This is because the southern model has smaller critical slip than the northern model. The effects of these parameters make the southern model rougher in high frequencies than the northern model.

In order to observe the effects of the faulting when the rupture breaks the surface, in Figure 13 we compare the final displacements and the peak velocities on the surface from two dynamic source models: one is the southern model shown in Figure 7a in which the rupture reaches the ground

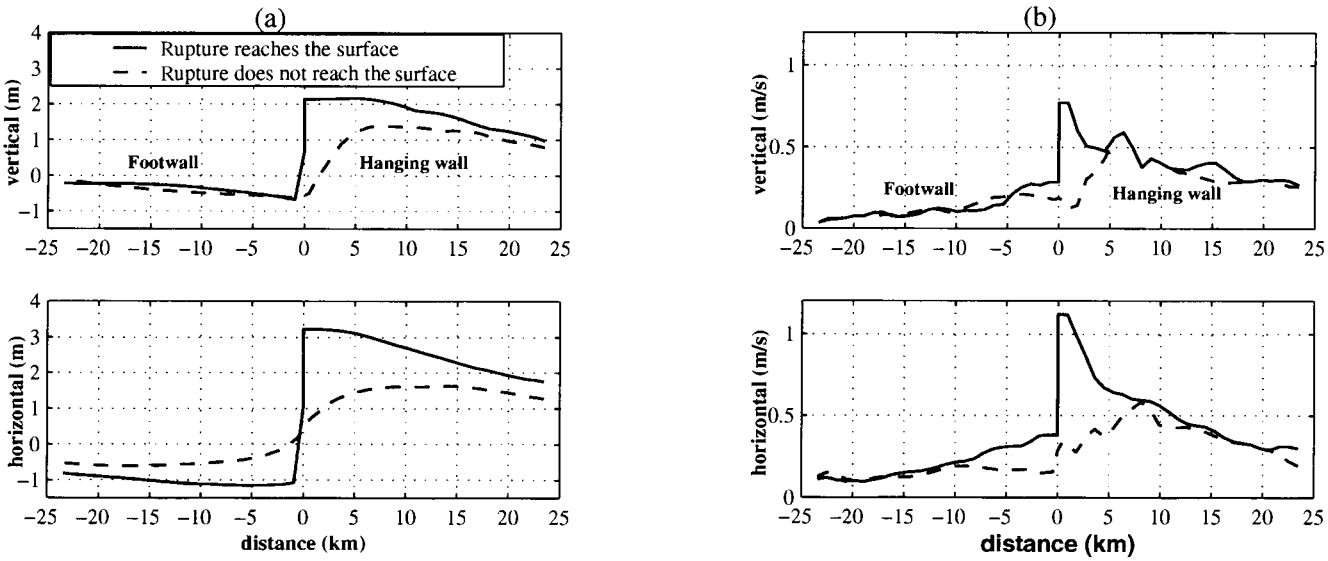

Figure 13. Comparison between the southern model used to simulate the 1999 Chi-Chi earthquake in which the rupture breaks the surface (solid line), and another model in which the rupture does not reach the surface (dashed line): (a) vertical and horizontal component of the final displacement along the surface, and (b) vertical and horizontal component of peak velocity along the surface.

surface (solid line), and the other one is a similar model in which the rupture is forced to stop 3 km before it reaches the surface (dashed line). It can be clearly observed that when the rupture reaches the surface there is a strong effect on the ground motions very close to the surface trace. The ground motion is enhanced when the rupture breaks the ground surface.

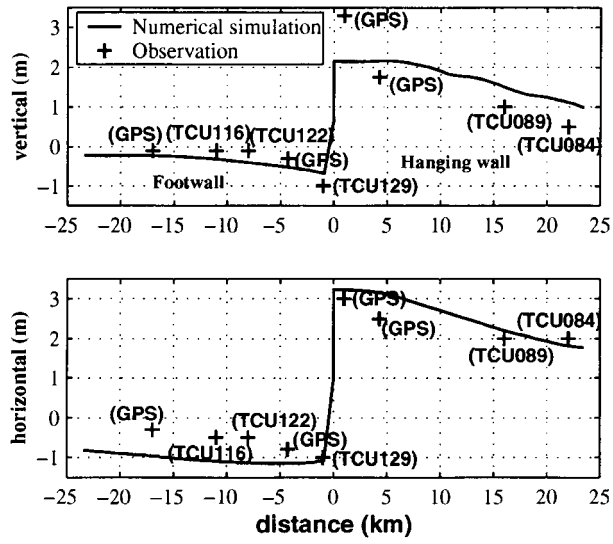

Figure 14. Comparison between the numerical simulation and the observations (GPS data and stations records) of the final displacements along the surface near the epicentral area (southern model).

In order to validate the dynamic model studied here, we compared our results of the southern model with the observations. Figure 14 shows that the southern model predicts final vertical displacement of about 2.0 m and horizontal displacement of about 3.3 m in the hanging wall that agree satisfactorily with those obtained by the Global Positioning System (GPS) data and the final displacements of the station records. In Figure 15a–e we also compare the waveform of the displacement and velocity ground motions of east–west and vertical components recorded at five stations near the surface rupture of the epicentral area (stations TCU084 and TCU089 on the hanging-wall side and TCU129, TCU116, and TCU122 on the footwall side). We find that the main characteristics of the recorded ground motion are adequately reproduced, as observed in the simulated and observed time histories. In the frequency range from 0.5 to 1.0 Hz, although obtained with a 2D model, the ground-motion simulation qualitatively matches the observations. The simulations for stations TCU084 and TCU089, located on the hanging wall,

Figure 15. Comparison of the numerical simulation with stations records of horizontal (E–W) and vertical component of displacement, velocity, and velocity in frequency range of 0.5–1.0 Hz: (a) for TCU084 station, (b) for TCU089 station, (c) for TCU129 station, (d) for TCU122 station, (e) for TCU116 station, (f) TCU052 station. *Dh* and *Dv* are the horizontal (east-west) and vertical components, respectively, and *Vh* and *Vv* are the horizontal (east–west) and vertical component of velocity ground motion, respectively.

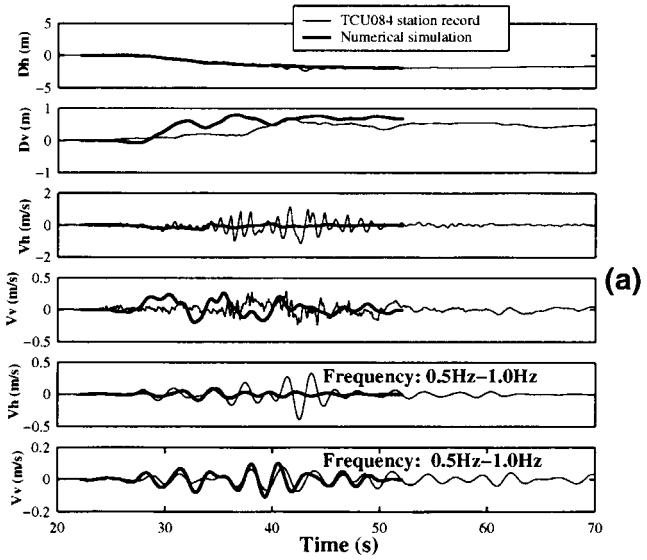
TCU084 station record
Numerical simulation
Dh (m)
Dv (m)
Vh (m/s)
Vv (m/s)
Frequency: 0.5Hz–1.0Hz
Frequency: 0.5Hz–1.0Hz
Time (s)

(a)

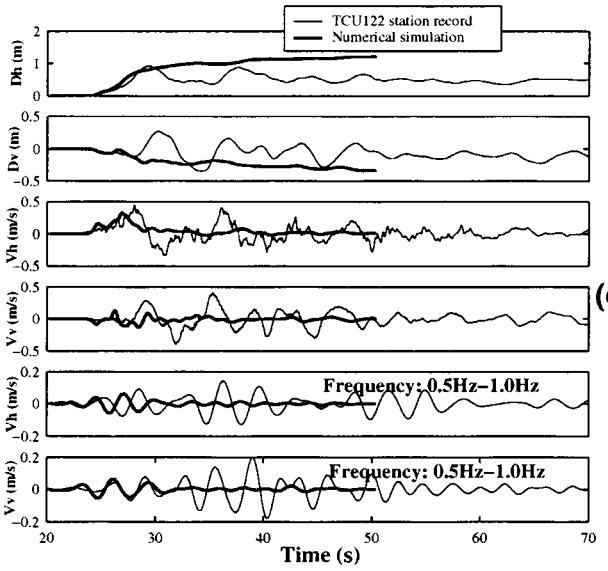
TCU122 station record
Numerical simulation
Dh (m)
Dv (m)
Vh (m/s)
Vv (m/s)
Frequency: 0.5Hz–1.0Hz
Frequency: 0.5Hz–1.0Hz
Time (s)

(d)

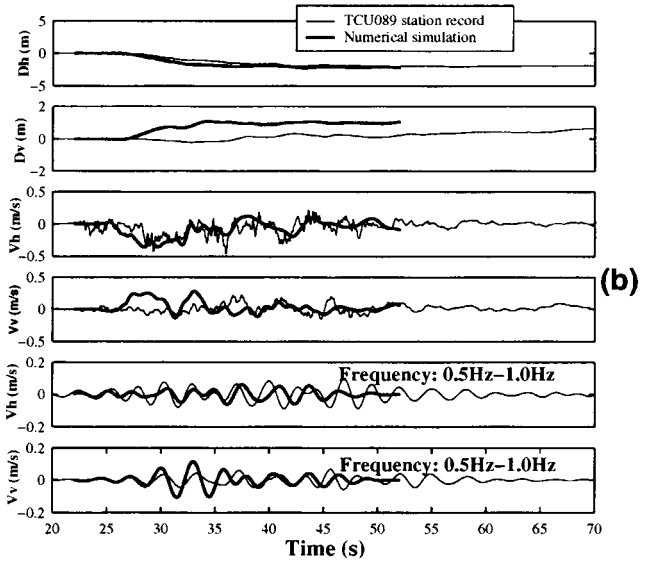
TCU089 station record
Numerical simulation
Dh (m)
Dv (m)
Vh (m/s)
Vv (m/s)
Frequency: 0.5Hz–1.0Hz
Frequency: 0.5Hz–1.0Hz
Time (s)

(b)

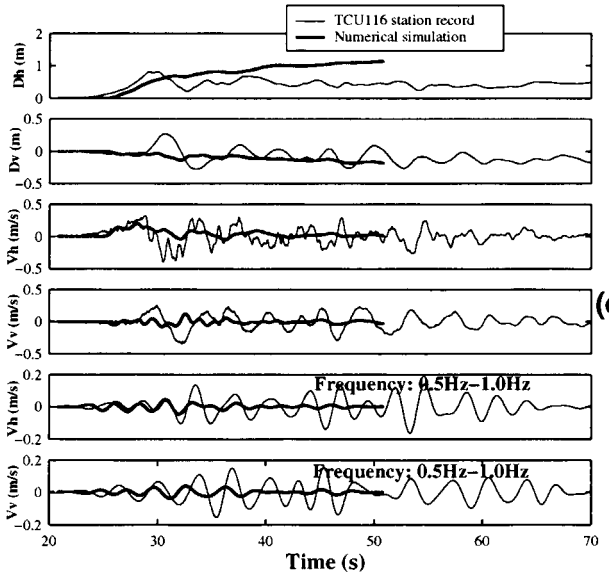
TCU116 station record
Numerical simulation
Dh (m)
Dv (m)
Vh (m/s)
Vv (m/s)
Frequency: 0.5Hz–1.0Hz
Frequency: 0.5Hz–1.0Hz
Time (s)

(e)

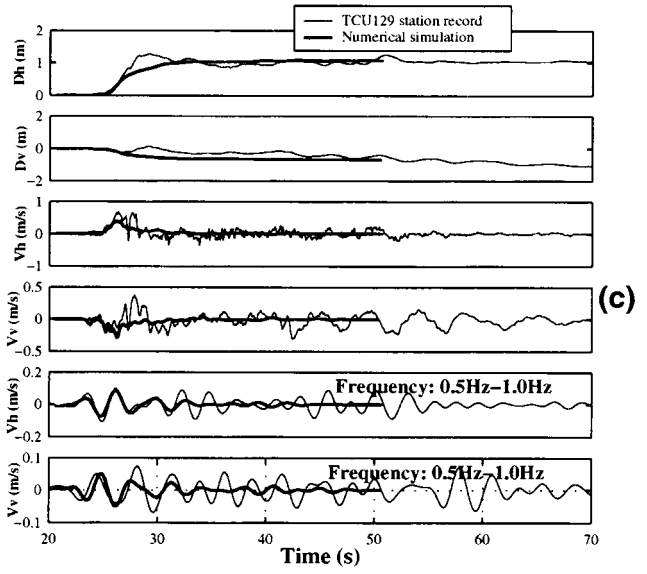
TCU129 station record
Numerical simulation
Dh (m)
Dv (m)
Vh (m/s)
Vv (m/s)
Frequency: 0.5Hz–1.0Hz
Frequency: 0.5Hz–1.0Hz
Time (s)

(c)

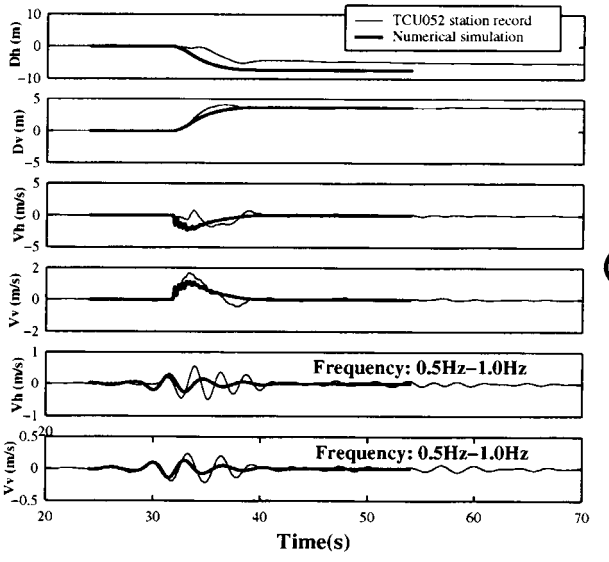
TCU052 station record
Numerical simulation
Dh (m)
Dv (m)
Vh (m/s)
Vv (m/s)
Frequency: 0.5Hz–1.0Hz
Frequency: 0.5Hz–1.0Hz
Time(s)

(f)

fit the observations well, except for the horizontal component of the TCU084 station, which, according to Chiu (2000), has noticeable site effects in the horizontal component. On the other hand, the simulations for stations TCU129, TCU122, and TCU116, located on the footwall side, agree well with the observed motion only in the initial part of the complete time histories. The ground motion on the footwall side was maybe influenced by softer surface-layer effects that are not taken into account in our simulation.

The simulation of the ground-motion records by means of a 2D model is more feasible for the southern model because herein the 3D effects would be smaller in relation to the geometry from the hypocenter to the site. Consequently we can in such case perform a robust simulation using a simplified 2D model. On the other hand, we believe that the northern part was strongly affected by the 3D effects, rendering the 2D ground-motion simulation records highly questionable. In this context, the dynamic rupture simulation of the northern model fault was carried out just to allow some comparisons with the southern part, in connection with the damage distribution, which is the objective of this article. But even with the limitation of the northern model mentioned previously, we succeeded in simulating the ground motion recorded at TCU052 station, as shown in Figure 15f, in which the simulation closely fits the recorded motion. This is because this station is located very close to the fault on the hanging wall, as shown in Figures 1 and 7b, where the dislocation of the fault is clearly recorded in the data.

Conclusions

Certainly there will be widespread disagreement on the possibility of representing a complex earthquake such as the 1999 Chi-Chi, Taiwan, earthquake by means of a simple 2D model. We want to stress that our intention was not to fully simulate the rupture process of the fault nor the resulting ground motions, for which purpose a complete 3D model would be needed, but to provide some interpretation of the distribution of damage on structures caused by the earthquake, based on the dynamic rupture process.

Using the simplified 2D DEM, it was possible to show some aspects of the dynamic source effects on the strong ground motion of the 1999 Chi-Chi earthquake. The ground-motion simulation of the southern model has a satisfactory agreement with the observed records. Also, even with the limitation of the northern model to simulate ground-motion records, the comparison of the simulation with the TCU052 station record is very good. These comparisons with the observations provide the validity of the results presented in this article.

The results show that the velocity ground motions in the northern part (hanging wall) in the frequency range of 0.5–2 Hz (natural frequency range of standard structures) are small near the surface break, thus, light structural damage might be predicted near the surface rupture. The model of the southern part presents smaller displacements and smaller velocity ground motions than the model at the northern part. As discussed before, in spite of this global difference, the ground motion in the southern part, in the frequency range of 0.5–2 Hz, is larger than in the north. Moreover, the fault rupture propagation reaches to surface with a very slow velocity (about 1.2 km/sec) in the northern part. However, in the southern part, it reaches the surface with considerable higher velocity (a supersonic velocity of about 3.0km/sec). The supersonic rupture velocity is a controversial issue. In our simulation, supersonic velocity is observed near the free surface in the southern model because we use small strength excess and small D_c. These values were adopted in order to generate higher frequency ground motion than in the northern model. In this context, the near source high frequency ground motion actually observed in the strong-motion data could be caused by possible supersonic rupture velocity in the southern zone of the Chi-Chi earthquake.

These results suggest that the ground motion near the fault of the 1999 Chi-Chi earthquake was affected mainly by dynamic source effects. These source effects predict stronger ground motions in the north for lower frequencies. However, for higher frequencies, between 0.5 and 2.0 Hz, the ground motion was predicted to be stronger in the southern model. From these results we can conclude that even though the northern model shows stronger ground motion, the most severe damage to structures should be expected in the south because it has a greater potential to severely excite the fundamental mode of most standard, low height structures. The model presented in this article clearly shows that dynamic effects of the source mechanism on strong ground motion prediction are of fundamental importance for the assessment of seismic hazard.

Acknowledgments

We are thankful to the Seismology Center, Central Weather Bureau (CWB), Taipei, Taiwan, for providing the Digital waveform files corresponding to the accelerograms of the stations used, and to Prof. Kuo-Liang Wen from the Office of the National Science and Technology Program for Hazards Mitigation, Taipei, Taiwan, for his cooperation in releasing information on structural damage and population distributions population distribution along the causative fault. We express our sincere thanks to the reviewers for constructive criticism and valuable suggestions. This research was supported by a Grant-in-Aid for Science Research, No. 11792026, from the Ministry of Education, Science, Sports and Culture of Japan, and by the National Council for Scientific and Technological Development (CNPq) of Brazil.

References

Andrews, D. J. (1976). Rupture velocity of plane-strain shear cracks, *J. Geophys. Res.* **81,** 5679–5687.

Brune, J. N. (1996). Particle motion in a physical model of shallow angle thrust faulting, *Proc. Indian. Cad. Sci.* **105,** 197–206.

Chiu, Hung-Chie (2000). Strong ground motion records from the 1999 Chi-Chi earthquake, unpublished document, Institute of Earth Science, Academia Sinica, Taipei, Taiwan.

Cochard, A., and R. Madariaga (1994). Dynamic Faulting Under Rate-Dependent Friction, *PAGEOPH* **142,** 419–445.

Dalguer, L. A., J. D. Riera, and K. Irikura (1999). Simulation of seismic excitation using a stick-slip source mechanism, Transaction, 15th International Conference on Structural Mechanics in Reactor Technology (SMiRT15), Seoul, Korea, August 1999, VIII, 13–18.

Dalguer, L. A., K. Irikura, J. D. Riera, and H. C. Chiu (2001). Fault dynamic rupture simulation of the hypocenter area of the thrust fault of the 1999 Chi-Chi (Taiwan) Earthquake, *Geophys. Res. Lett.* **28,** 1327–1330.

Das, S., and K. Aki (1977). A numerical study of two-dimensional spontaneous rupture propagation, Geophys. J. R. Astr. Soc. **50,** 643–668.

Day, S. M. (1982a). Three-dimensional finite difference simulation of fault dynamics: rectangular fault with fixed rupture velocity, *Bull. Seism. Soc. Am.* **72,** 705–727.

Day, S. M. (1982b). Three-dimensional simulation of spontaneous rupture: the effect of nonuniform prestress, *Bull. Seism. Soc. Am.* **72,** 1881–1902.

Dieterich, J. H. (1979). Modeling of Rock Friction, Part I. Experimental Results and Constitutive Equation, *J. Geophys. Res.* **84,** 2161–2168.

Doz, G. N., and J. D. Riera (1995). Towards the numerical simulation of seismic excitation, Transaction, 13th International Conference on Structural Mechanics in Reactor Technology (SMiRT13), Porto Alegre, Brazil, August 1995, III.

Fukuyama, E., and R. Madariaga (1998). Rupture dynamics of a planar fault in a 3D elastic medium: rate- and slip-weakening friction, *Bull. Seism. Soc. Am.* **88,** 1–17.

Guatteri, M., and Spudich, P. (2000). What can strong-motion data tell us about slip-weakening fault-friction laws? *Bull. Seism. Soc. Am.* **90,** 98–116.

Harris, R. A., and S. M. Day (1999). Dynamic 3D simulations of earthquakes on en echelon faults, *Geophys. Res. Lett.* **26,** 2089–2092.

Ida, Y. (1972). Cohesive force across the tip of a longitudinal-shear crack and Griffith's specific surface energy, *J. Geophys. Res.* **77,** 3796–3805.

Ide, S., and Takeo M. (1997). Determination of constitutive relations of fault slip based on seismic wave analysis, *J. Geophys. Res.* **102,** 27379–27391.

Inoue, T., and T. Miyatake (1998). 3D simulation of near-field strong ground motion based on dynamic modeling, *Bull. Seism. Soc. Am.* **88,** 1445–1456.

Iwata, T., H. Sekiguchi, and K. Irikura (2000). Source process of the 1999 Chi-Chi, Taiwan, earthquake and its near-fault strong ground motion, 2000 Western Pacific Geophysics Meeting (supplement) *EOS Trans. Am. Geophys. Union* **81,** WP144, S51F-02 (abstract).

Kostrov, B. V. (1964). Self-similar problem of propagation of shear crack, *J. Appl. Math. Mech.* **28,** 1077–1087.

Kostrov, B. V. (1966). Unsteady propagation of longitudinal shear cracks, *J. Appl. Math. Mech.* **30,** 1241–1248.

Ma, K. F., and J. Mori (2000). Rupture process of the 1999 Chi-Chi, Taiwan, earthquake from direct observations and joint inversion of strong motion, GPS and teleseismic data, 2000 Western Pacific Geophysics Meeting, Tokyo, Japan, 27–30 June 2000 (supplement) (abstract) *EOS Trans. Am. Geophys. Union* **81,** WP104, S21A-07.

Madariaga, R., K. Olsen, and R. Archuleta (1998). Modeling dynamic rupture in a 3D earthquake fault model, *Bull. Seism. Soc. Am.* **88,** 1182–1197.

Marone, C., and Kilgore, B. (1993). Scaling of the critical slip distance for seismic faulting with shear strain in fault zone, *Nature* **362,** 618–621.

Mikumo, T., and T. Miyatake (1978). Dynamical rupture process on a three-dimensional fault with non-uniform frictions and near-field seismic waves, *Geophys. J. R. Astr. Soc.* **54,** 417–438.

Mikumo, T., and T. Miyatake (1993). Dynamic rupture processes on dipping fault, and estimates of stress drop and strength excess from the results of waveform inversion, *Geophys. J. Int.* **112,** 481–496.

Mora, P., and D. Place (1994). Simulation of the frictional stick-slip instability, *PAGEOPH* **143,** 61–87.

Nayfeh, A. H., and M. S. Hefsy (1978). Continuum modeling of three-dimensional truus-like space structures, *AIAA J.* **16,** 779–787.

Nielsen, S. B. (1998). Free surface effects on the propagation of dynamic rupture, *Geophys. Res. Lett.* **25,** 125–128.

Oglesby, D. D., R. J. Archuleta, and S. B. Nielsen (1998). Earthquakes on dipping faults: the effects of broken symmetry, *Science* **280,** 1055–1059.

Oglesby, D. D., R. J. Archuleta, and S. B. Nielsen (2000). The three-dimensional dynamics of dipping faults, *Bull. Seism. Soc. Am.* **90,** 616–628.

Ohnaka, M. (1992). Earthquake source nucleation: a physical model for short term precursors, *Tectonophysics* **211,** 149–178.

Ohnaka, M., Y. Kuwahara, and K. Yamamoto (1987). Constitutive relations between dynamic physical parameters near a tip of the propagating slip zone during stick-slip shear failure, *Tectonophysics* **144,** 109–125.

Olsen, K., R. Madariaga, and R. Archuleta (1997). Three-dimensional dynamic simulation of the 1992 Landers earthquake, *Science* **278,** 834–838.

Riera, J. D. (1982) Basic concepts and load characteristics in impact problems, in *Concrete Structures under Impact and Impulsive Loading,* Introductory report, RILEM, CEB, IABSE, IASS-Interassociation Symposium, Berlin, June 1982, 7–29.

Riera, J. D., and M. Rocha (1991). A note on the velocity of crack propagation in tensile fracture, *Revista Brasileira de Ciencias Mecanicas, RBCM,* **XII,** no. 3, 217–240.

Rimal, M. H. (1992). Dynamic fracture analyses by the extended distinct element Method, *Doctoral Dissertation,* Department of Civil Engineering, University of Tokyo, Japan.

Ruina, A. (1983). Slip instability and state variable friction laws, *J. Geophys. Res.* **88,** 10359–10370.

Scholz, C. H. (1990). *The Mechanics of Earthquakes and Faulting,* Cambridge University Press, New York.

Shi, B., A. Anooshehpoor, J. N. Brune, and Y. Zeng (1998). Dynamics thrust faulting: 2D lattice model, *Bull. Seism. Soc. Am.* **88,** 1484–1494.

Shin, T. C., K. W. Kuo, W. H. K. Lee, T. L. Teng, and Y. B. Tsai (2000). A preliminary report on the 1999 Chi-Chi (Taiwan) Earthquake, *Seism. Res. Lett.* **71,** 24–30.

Tsai, Y. B., and M. W. Huang (2000). Strong ground motion characteristics of the Chi-Chi, Taiwan earthquake of September 21, 1999, *Earthquake Eng. Eng. Seismology* **2,** 1–21.

Virieux, J., and R. Madariaga (1982). Dynamic faulting studied by a finite difference method, *Bull. Seism. Soc. Am.* **72,** 345–369.

Yagi, Y., and M. Kikuchi (2000). Source rupture process of the Chi-Chi, Taiwan, earthquake of 1999, obtained by seismic wave and GPS data, 2000 Western Pacific Geophysics Meeting, Tokyo, Japan, 27–30 June 2000 (supplement) (abstract), *LOS Trans. Am. Geophys. Union* **81,** WP104, S21A-05.

Appendix

Determination of the Equivalent Stiffness of the Normal and Diagonal Bars of the DEM

The determination of the equivalent axial stiffness of the elements in a cubic lattice array, as shown in Figure 4 (equations 1 and 2), in terms of the elastic properties of an equivalent isotropic continuum is reviewed here. This equivalence was shown by Nayfeh and Hefzy (1978) and first employed in dynamic problems by Riera (1982).

The stress-strain for a general elastic body may be written in the indicial notation form:

$$\sigma_i = C_{ij}\varepsilon_j, \quad i,j = 1 \ldots 6, \tag{A1}$$

where σ_i and ε_j are the independent six components of the stress and strain tensors, respectively, and C_{ij} are elastic constants, which are 21 independent constants on account of symmetry considerations.

For an isotropic material, the constants C_{ij} could be a function of only two independent constants, so C_{ij} can be ordered as:

$$C_{ij} = \begin{bmatrix} C_{11} & C_{12} & C_{12} & 0 & 0 & 0 \\ C_{12} & C_{11} & C_{12} & 0 & 0 & 0 \\ C_{12} & C_{12} & C_{11} & 0 & 0 & 0 \\ 0 & 0 & 0 & C_{44} & 0 & 0 \\ 0 & 0 & 0 & 0 & C_{44} & 0 \\ 0 & 0 & 0 & 0 & 0 & C_{44} \end{bmatrix}, \quad \text{(A2)}$$

in which C_{11}, C_{12}, and C_{44} are functions of Young's modulus E and the Poisson's ratio v.

Since the DEM implies a lattice-type structure consisting of one-dimensional axial elements, the contribution of each member to the overall stiffness must be duly accounted for the sum of the average contribution of each element will lead to the final stiffness matrix. It is assumed that the elements are perfectly straight and present constant cross-sectional area.

The elastic constants C_{ij} can be transformed from one orthogonal cartesian coordinates system x_i to another $\bar{x}_i$ (i = 1,2,3) through an expression:

$$\bar{Q}_{ij} = f(Q_{i,j},\ \alpha_{kl}) \begin{cases} (k,\ l = 1 \ldots 3a) \\ (i,\ j = 1 \ldots 6) \end{cases}, \quad \text{(A3)}$$

where α_n denotes the direction cosines of the transformation. Q_{ij} and $\bar{Q}_{ij}$ are the elastic constant of systems x and $\bar{x}$, respectively. The derivation of equation (A3) is presented in details in Nayfeh and Hefzy (1978).

Equation (A3) is used in order to get the coefficients of equation (A2) for the corresponding cubic model of Figure 4a. Since all elements have the single unidirectional property E, each set of parallel bars defines a continuum with a single effective unidirectional property, which we shall refer to as Q_{11}. In the context of effective modulus theories, Q_{11} will be an area-averaged modulus. Thus, the value of Q_{11} will depend not only upon the specific model under consideration but also upon the spacing of the bars.

In particular, the cubic array shown in Figure 4a has two different properties of Q_{11}, one corresponds to the elements normal to the face of the cube (Q^{n}_{11}), and the other corresponds to the diagonal elements (Q^{d}_{11}).

The unidirectional effective properties, Q^{n}_{11} and Q^{d}_{11}, can be determined by referring to the projected area normal to each element in order to obtain the effective area. For the normal elements, we can obtain an effective area equal to $L^2/2$, while for the diagonal elements it results in $L^2/\sqrt{3}$. Thus, the unidirectional property for each element is given by

$$Q^{\mathrm{n}}_{11} = \frac{2EA_{\mathrm{n}}}{L^2}, \quad \text{(A4)}$$

$$Q^{\mathrm{d}}_{11} = \frac{\sqrt{3}EA_{\mathrm{d}}}{L^2}, \quad \text{(A5)}$$

in which L is the side length of the basic cube, and EA_n and EA_{d} are Young's modulus E times the cross-sectional area A for the normal and diagonal elements, respectively.

From equations (A4) and (A5), $\bar{Q}_{ij}$ of equation (A3), that is, the stiffness constants of a continuum equivalent to the cubic lattice model may be obtained. As shown in Figure 4a, seven elements converge to each node of the cubic model (three normal and four diagonals bars), hence $\bar{Q}_{ij}$ can be expressed as follows:

$$\bar{Q}_{ij} = \sum_{I=1}^{3} f(Q^{\mathrm{n}}_{11},\ \alpha^{\mathrm{n}}_{Ikl}) + \sum_{J=1}^{4} f(Q^{\mathrm{d}}_{11},\ \alpha^{\mathrm{d}}_{Jkl}) \ (k,\ l = 1 \ldots 3), \quad \text{(A6)}$$

in which $\alpha^{\mathrm{n}}_{Ikl}$ and $\alpha^{\mathrm{d}}_{Jkl}$ are the direction cosines of the systems $\bar{x}$, $x^{\mathrm{n}}_{\mathrm{I}}$ and $\bar{x}$, x^{d}_{J}, respectively.

Combining equations (A4), (A5), and (A6), the elastic constants of equation (A2) can be obtained:

$$\begin{aligned} C_{11} &= Q^{\mathrm{n}}_{11}\left(1 + \frac{4}{9}\delta\right), \\ C_{12} &= Q^{\mathrm{n}}_{11}\left(\frac{4}{9}\delta\right), \\ C_{44} &= Q^{\mathrm{n}}_{11}\left(\frac{4}{9}\delta\right), \end{aligned} \quad \text{(A7)}$$

where

$$\delta = \frac{Q^{\mathrm{d}}_{11}}{Q^{\mathrm{n}}_{11}} = \frac{\sqrt{3}A_{\mathrm{d}}}{2A_{\mathrm{n}}}. \quad \text{(A8)}$$

Therefore, the constants C_{ij} of equation (A2) is:

$$C_{ij} = \frac{2EA_{\mathrm{n}}}{L^2} \begin{bmatrix} 1+\frac{4\delta}{9} & \frac{4\delta}{9} & \frac{4\delta}{9} & 0 & 0 & 0 \\ \frac{4\delta}{9} & 1+\frac{4\delta}{9} & \frac{4\delta}{9} & 0 & 0 & 0 \\ \frac{4\delta}{9} & \frac{4\delta}{9} & 1+\frac{4\delta}{9} & 0 & 0 & 0 \\ 0 & 0 & 0 & \frac{4\delta}{9} & 0 & 0 \\ 0 & 0 & 0 & 0 & \frac{4\delta}{9} & 0 \\ 0 & 0 & 0 & 0 & 0 & \frac{4\delta}{9} \end{bmatrix} \quad \text{(A9)}$$

The engineering elastic constants, Young's modulus E, Poisson's ratio v, and shear modulus μ may be expressed in terms of the constants C_{ij} using the general stress-strain re-

lations for anisotropic materials (Nayfeh and Hefzy, 1978), as follows:

$$E = C_{11} - \frac{2C_{12}^2}{C_{11} + C_{12}}, \tag{A10a}$$

$$v = \frac{C_{12}}{C_{11} + C_{12}}, \tag{A10b}$$

$$\mu = \frac{1}{2} C_{44}. \tag{A10c}$$

Substituting in equation (A9), we obtain:

$$E = \frac{2EA_n (9 + 12\delta)}{L^2(9 + 8\delta)}, \tag{A11a}$$

$$v = \frac{4\delta}{9 + 8\delta}, \tag{A11b}$$

$$\mu = \frac{EA_n 4\delta}{9L^2}. \tag{A11c}$$

To get the equivalent values of EA_n and EA_d as functions of the elastic properties of the material (which could be, for instance, E and v), we use equation (A11) and the relation given in equation (A8), as follows:

$$\delta = \frac{9v}{(4 - 8v)}, \tag{A12a}$$

$$EA_n = \frac{L^2(9 + 8\delta)}{2(9 + 12\delta)} E, \tag{A12b}$$

$$EA_d = \frac{\delta L^2(9 + 8\delta)}{\sqrt{3}(9 + 12\delta)} E. \tag{A12c}$$

Finally, the equivalent stiffness of the normal and diagonal elements is obtained dividing equations (A12a,b) by the length of the respective element, being $L_n = L$ (for normal elements) and $L_d = \sqrt{3}/2\ L$ (for diagonal elements):

$$\frac{EA_n}{L_n} = \frac{L(9 + 8\delta)}{2(9 + 12\delta)} E \tag{A13a}$$

$$\frac{EA_d}{L_d} = \frac{2\ \delta L(9 + 8\ \delta)}{3(9 + 12\ \delta)} E \tag{A13b}$$

The nodal masses, m_i, are calculated in terms of the volumes of influence of each node i, for the internal nodes it results:

$$m_i = \frac{\rho L^3}{2} \tag{A14}$$

while for surface nodes, linear corner, and point corner nodes, the mass given by equation (A14) must be divided by 2, 4, and 8, respectively.

Disaster Prevention Research Institute
Kyoto University
Gokasho, Uji, Kyoto 611-0011, Japan
dalguer@egmdpri01.dpri.kyoto-u.ac.ip
(L.A.D.)

Curso de Pós Graduação de Engenharia Civil
Universidade Federal de Rio Grande do Sul
Av. Osvaldo Aranha 99, 3° andar, CEP 90035-190
Porto Alegre, R.S. Brazil
dalguer@vortex.ufrgs.br
(L.A.D.)

Disaster Prevention Research Institute
Kyoto University
Gokasho, Uji, Kyoto 611-0011, Japan
irikura@egmdpri01.dpri.kyoto-u.ac.ip
(K.I.)

Curso de Pós Graduação de Engenharia Civil
Universidade Federal de Rio Grande do Sul
Av. Osvaldo Aranha 99, 3° andar, CEP 90035-190
Porto Alegre, R.S. Brazil
riera@genesis.cpgec.ufrgs.br
(J.D.R.)

Institute of Earth Science
Academia Sinica, Nankang, Taipei, Taiwan
chiu@earth.sinica.edu.tw
(H.C.C.)

Manuscript received 31 July 2000.